Enhanced energy-storage in lead-free multilayer capacitors via entropy-assisted polymorphic domain engineering

Jiaqi Li [1,2,5], Yibing Zhang[1,5], Zhen Liu [2] ✉, Lingling Wei[3], Haonan Peng[2], Minghao Liu[2], Shiguang Yan[2], Kunyu Zhao[2], Huarong Zeng [2] ✉, Zupei Yang [1] ✉ & Genshui Wang [2,4] ✉

Lead-free multilayer ceramic capacitors with high energy storage performance are essential components in environmentally sustainable and miniaturized pulsed power systems. However, their practical application is limited by inherently low energy density and suboptimal energy efficiency. In this study, a stepwise dual-site entropy increase strategy is introduced to simultaneously modulate relaxor behavior and enhance the breakdown strength of $Bi_{0.5}Na_{0.5}TiO_3$-based capacitors. Atomic-scale structural analyses reveal that the coexistence of rhombohedral, tetragonal, and cubic polymorphic domains effectively prevents premature polarization saturation while maintaining high maximum polarization. Additionally, the high configurational entropy induces non-periodic lattice distortions, promoting grain refinement and improving electrical resistance, which collectively enhance breakdown endurance. Consequently, an enhanced energy density of 17.8 J cm^{-3} with a high efficiency of 97.6% is achieved in the high-entropy capacitors. Furthermore, the high-entropy capacitors exhibit excellent thermal and fatigue stability, along with superior charge-discharge performance. This study provides a viable structural design approach for developing high-performance relaxor ferroelectric materials and devices with optimized energy storage characteristics.

Multilayer ceramic capacitors (MLCCs) demonstrate exceptional power density and ultrafast charge-discharge characteristics. These features make them crucial components in pulse power systems, which find significant applications in sectors such as electric vehicles, portable electronics, and medical devices[1–3]. However, the typically low recoverable energy density (W_{rec}) and/or energy efficiency (η) of MLCCs present challenges to the miniaturization, integration, and lightweight design of devices[4]. Energy storage performance (ESP) of capacitors is commonly assessed through their polarization-electric field (P-E) hysteresis loop, calculated as follows[5]: $W_{total} = \int_0^{P_m} EdP$, $W_{rec} = \int_{P_r}^{P_m} EdP$, $\eta = \frac{W_{rec}}{W_{total}} \times 100\%$, where P_m and P_r represent the maximum and remanent polarization, respectively. Therefore, achieving significant polarization variation ($\Delta P = P_m$-P_r), high dielectric breakdown strength (E_b), and delayed polarization saturation is essential for advancing high-ESP MLCCs.

Relaxor ferroelectrics (RFEs) have been extensively studied as promising candidates for achieving high ESP due to their characteristic narrow hysteresis loops, large ΔP, and high E_b[6–8]. The remarkable ESP

[1]School of Material Science and Engineering, Shaanxi Normal University, Xi'an, China. [2]Key Laboratory of Inorganic Functional Materials and Devices, Shanghai Institute of Ceramics, Chinese Academy of Sciences, Shanghai, China. [3]School of Chemistry and Chemical Engineering, Shaanxi Normal University, Xi'an, China. [4]The State Key Laboratory of High Performance Ceramics and Superfine Microstructure, Shanghai Institute of Ceramics, Chinese Academy of Sciences, Shanghai, China. [5]These authors contributed equally: Jiaqi Li, Yibing Zhang. ✉e-mail: zhenliu@mail.sic.ac.cn; huarongzeng@mail.sic.ac.cn; yangzp@snnu.edu.cn; genshuiwang@mail.sic.ac.cn

in RFEs primarily arises from the dynamic response of polar nanoregions (PNRs), which effectively suppresses the remanent polarization (P_r) by lowering the polarization switching barrier[9]. However, further enhancement of ESP in RFE ceramics faces two key challenges. First, the coupling effects between PNRs generate enhanced local electric fields that drive cooperative switching, leading to premature polarization saturation[10], significantly restricting the improvement of W_{rec}. Second, while high P_m is essential for achieving high ESP, RFEs with high P_m usually exhibit localized stress and strain concentrations under high electric fields, leading to compromised reliability and reduced E_b[11]. This interdependent relationship between P_m and E_b hinders the achievement of high W_{rec}.

Recently, the high-entropy design strategy has emerged as a promising approach to address these fundamental limitations, leading to significant improvements in ESP across various materials, including bulk ceramics (W_{rec} of 11.0 J cm^{-3} and η of 81.9%)[12], MLCCs (W_{rec} of 20.8 J cm^{-3} and η of 97.5%)[13], and thin films (W_{rec} of 182 J cm^{-3} and η of 78%)[14]. The atomic configuration entropy (S_{config}) can be determined as follows: $S_{config} = -R \left[\left(\sum_{i=1}^{N} x_i \ln x_i \right)_{cation-site} + \left(\sum_{j=1}^{M} x_j \ln x_j \right)_{anion-site} \right]$, where R, N (M), and x_i (x_j) represent the ideal gas constant (8.314 J (K·mol)$^{-1}$), atomic species, and their respective contents[15], and has been proposed to evaluate the local compositional inhomogeneities, which are considered the origin of PNRs[16]. However, current high-entropy design approaches are primarily limited to single lattice sites, specifically either the A-site or the B-site, failing to fully exploit the potential of high-entropy optimization[17,18]. Unlike high-entropy alloys, the cation displacement in high-entropy ABO$_3$ oxide ceramics is constrained by the neighboring sublattice cations and the oxygen octahedral environment, preventing the random distortion degree of the designed high-entropy A- or B-sublattice site. This structural restriction suppresses global cation/structure disorder and therefore weakens the random distribution of orientation and magnitude of cation displacement. Such constraint behavior induces a coupling effect between the PNRs, thereby promoting easier polarization saturation. This coupling can be effectively disrupted/weakened by introducing further atomic disorder at secondary sites, thereby delaying saturation polarization. Therefore, a dual-site high-entropy design that incorporates both A-site and B-site may demonstrate enhanced efficacy in promoting greater structural disorder and a more gradual approach to saturated polarization. On the other hand, for the purpose of inducing beneficial structural distortion, the single-site high-entropy design generally necessitates the introduction of a high concentration of various cations with greater chemical differences. This often brings up difficulties in obtaining phase-pure high-entropy materials[19]. Through eliminating the mutual inhibition of A- and B-sites, the dual-site high-entropy design potentially offers a more efficacy approach to realize cation disorder and thus reduces the required doping concentration, which is favorable for the synthesis of phase-pure high-entropy ferroelectrics.

Here, we propose a novel stepwise dual-site entropy-increase strategy for the development of high ESP Bi$_{0.5}$Na$_{0.5}$TiO$_3$ (BNT) -based MLCCs (Fig. 1a and Tab. S1). The proposed design strategy consists of two sequential steps. First, Sr^{2+} and La^{3+} were incorporated at the A-site to induce moderate atomic disorder, forming a medium-S_{config} (Bi$_{0.3}$Na$_{0.3}$Sr$_{0.28}$La$_{0.08}$)TiO$_3$ (BNSLT, 1.29 R) component. Second, Mg^{2+} and Zr^{4+} were strategically introduced at the B-site to achieve a high-S_{config} (Bi$_{0.3525}$Na$_{0.2775}$Sr$_{0.259}$La$_{0.074}$)(Ti$_{0.925}$Mg$_{0.0375}$Zr$_{0.0375}$)O$_3$ (BNSLTMZ, 1.60 R) component. This synergistic dual-site entropy-assisted engineering facilitated greater structural disorder and achieved the coexistence of rhombohedral (R), tetragonal (T), and cubic (C) polymorphic domains, accompanied by non-periodic lattice distortion. The engineered material exhibited a significant reduction in dielectric loss, effectively mitigated premature polarization saturation, and demonstrated remarkable improvements in E_b and P_m.

Consequently, the high-S_{config} BNSLTMZ MLCCs exhibited excellent ESP, including a high W_{rec} of 17.8 J cm^{-3} and an excellent η of 97.6%. This approach not only offers a promising candidate device but also underscores the substantial efficacy of the proposed method in the design of next-generation energy storage ferroelectrics for practical applications.

Results and discussion

Energy-storage capability of entropy-assisted MLCCs

The dimensions of the BNSTMZ MLCCs were 3.0 × 2.4 × 0.3 mm (length × width × height), with four effective dielectric layers (Fig. S1). Figure 1b presents a digital photograph, a cross-sectional scanning electron microscopy (SEM) image, and energy dispersive spectrometer (EDS) mappings of the fabricated entropy-assisted MLCCs. The device exhibited a dense microstructure with well-defined dielectric-electrode interfaces, along with distinct elemental distributions corresponding to each layer. Notably, the sustained slender loops and low P_r under increasing electric fields enable these highly-reliable MLCCs to achieve both steadily enhanced W_{rec} and exceptionally stable η (Fig. 1c, d). Consequently, under an electric field of 125 kV mm^{-1}, the MLCCs demonstrated an excellent W_{rec} of 17.8 J cm^{-3} with a high η of 97.6%. This great ESP surpassed that of most recently reported state-of-the-art lead-free MLCCs, as illustrated in Fig. 1e[11,13,20–35]. Meanwhile, the MLCCs exhibited a good normalized energy storage density at high electric field, as defined by W_{rec}/E (Fig. S2)[36]. Furthermore, the entropy-assisted MLCCs also demonstrated excellent figure of merit ($U_F = W_{rec}/(1-\eta)$)[30], reaching 742. This excellent overall performance surpassed the best-performing lead-based systems and other state-of-the-art lead-free MLCCs by a considerable margin. (Fig. 1f). This positions our material among the top-performing dielectric capacitors, with the unique advantage of simultaneously maintaining both high W_{rec} and η at competitive levels.

Effect of dual-site entropy-increase strategy

To elucidate the effects of our dual-step entropy-increase strategy on BNT-based materials, we initially recorded the P-E loops of the BNT, BNSLT, and BNSLTMZ bulk ceramics to evaluate their ESP. The undoped BNT ceramics exhibited characteristic square ferroelectric hysteresis loops, whereas the BNSLT ceramics displayed elongated loops, indicative of relaxor behavior (Fig. S3)[37]. Quantitative analysis indicates that the substantial reduction in P_r in BNSLT ceramics led to a significant enhancement of the ΔP by over 6-fold and η by more than 9-fold compared to pristine BNT ceramics (Fig. 2b), achieving a W_{rec} of 5.2 J cm^{-3} and an η of 85.4% (Fig. S4). These results demonstrate that increasing atomic disorder at the A-site can effectively modulate the relaxor behavior of BNT-based ceramics. However, the A-site entropy-assisted design fails to achieve a sufficiently high E_b and is prone to premature polarization saturation, both of which limit further improvements in ESP. In contrast, the high-S_{config} BNSLTMZ ceramics exhibited significantly delayed polarization saturation and a significantly enhanced E_b of 80 kV mm^{-1}, while maintaining a high η. Consequently, a more than 2-fold enhancement in W_{rec} was achieved compared to the BNSLT ceramics (Fig. 2b). This optimization resulted in an impressive W_{rec} of 12.1 J cm^{-3} and a high η of 89.2% (Fig. S4). The exceptional ESP of BNSLTMZ bulk ceramics surpassed that of most recently reported lead-free RFE ceramic materials (Fig. S5), highlighting the effectiveness of our dual-site entropy-increase design for developing high-ESP MLCCs.

To probe the entropy-assisted structural evolution, the crystal structures of the BNT, BNSLT, and BNSLTMZ ceramics were subsequently analyzed. Rietveld refinements conducted on high-quality X-ray diffraction (XRD) data (R_{wp} < 5%, Fig. 2c and S6) indicate that the increase in entropy resulted in a significant decrease in the proportion of the polar R *R3c* phase, from 100% to 35%, and to 15%. Concurrently, with the entropy of the system increasing sequentially across the three
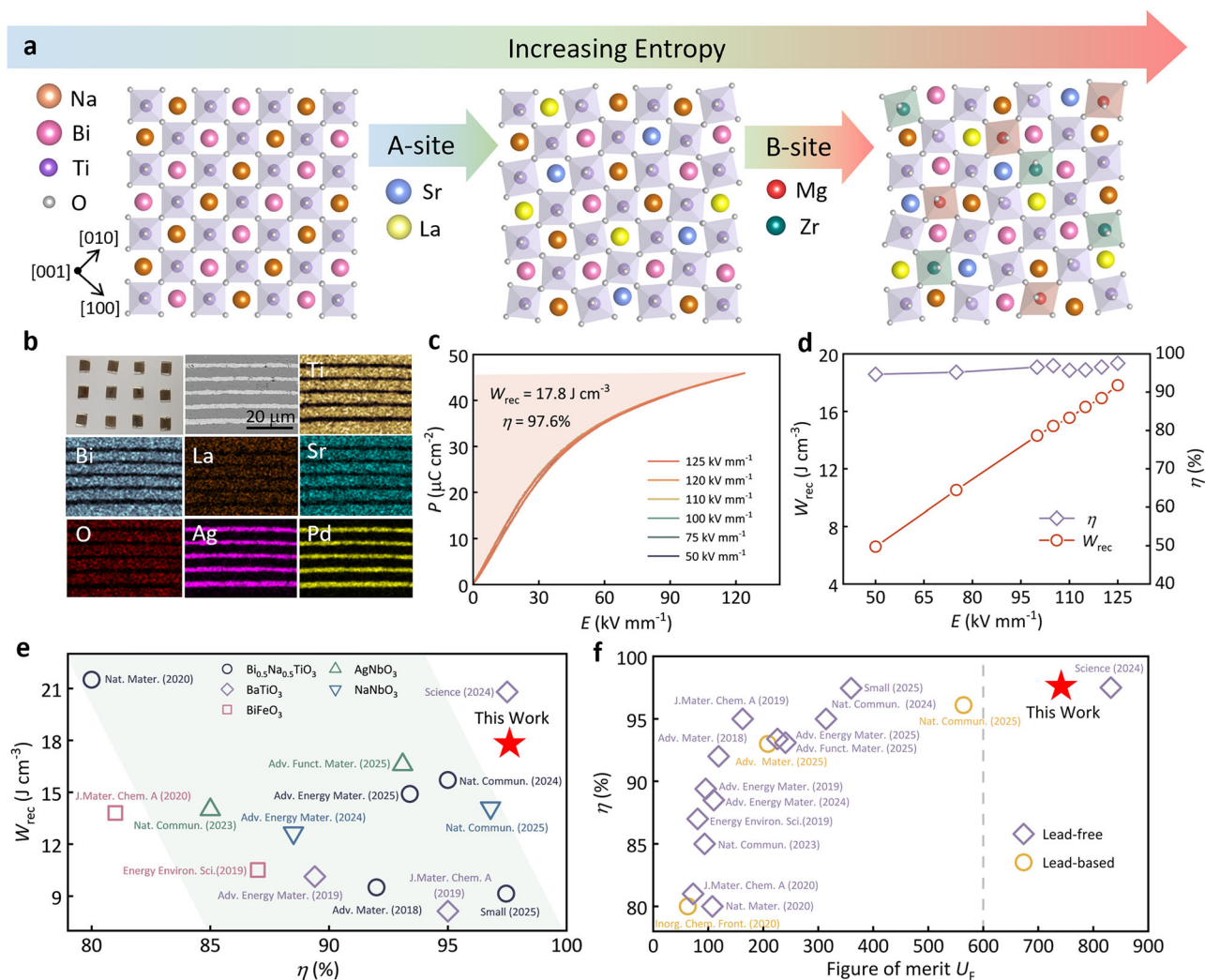
Fig. 1 | Stepwise entropy-increase strategy achieved ultrahigh ESP in MLCCs.
a Schematic diagram of the BNT-based components constructed based on the entropy-increase strategy. **b** Digital photograph, cross-sectional SEM image, and EDS mappings of the MLCCs. **c** Unipolar *P-E* loops of MLCCs as a function of applied *E*. **d** W_{rec} and η of the MLCCs as a function of applied *E*. The comparison of (**e**) W_{rec} and η, (**f**) η and U_F of the MLCCs with those of other recently reported state-of-the-art MLCCs.

components, the proportion of the non-polar/weakly polar T *P4bm* phase showed a stepwise rise, rising from 0% to 68%, and to 85% (Fig. 2d and Tab. S2). Complementary evidence for this dual-phase coexistence and its evolution was provided by Raman spectroscopy. Both the BNSLT and BNSLTMZ ceramics showed different peaks at 165 cm^{-1}, which correspond to the A$_2$(LO) mode of the *P4bm* phase (red region in Fig. 2c)[38], and peaks at 585 cm^{-1}, associated with the E(LO8) mode of the *R3c* phase (blue region in Fig. 2c)[39]. Additionally, an enhancement of the peaks at approximately 520 cm^{-1} was observed, accompanied by a reduction in the intensity of the peak at 585 cm^{-1}, providing compelling evidence for phase evolution in response to increased entropy. Furthermore, the peak at approximately 265 cm^{-1}, corresponding to the F$_{2g}$ mode of Ti-O vibrations[40], exhibited broadening and a red shift following the incorporation of Sr^{2+} and La^{3+} at the A-site, suggesting cationic disorder and a weakening of Ti–O bonds. Subsequent introduction of Mg^{2+} and Zr^{4+} at the B-site resulted in a blue shift of the F$_{2g}$ peak, indicating enhanced B–O bond strength and improved structural stability[41]. This enhancement contributes to increased electrical resistance and E_b.

Figures S7 and 2f, g illustrate the temperature-dependent dielectric constant and loss tangent of the BNT, BNSLT, and BNSLTMZ ceramics, measured across various frequencies. Two dielectric

anomalies were identified for all three compositions, with the corresponding temperatures T_s and T_m, which are associated with the thermal evolution of PNRs exhibiting *R3c* and *P4bm* symmetries[42,43]. The entropy-increase strategy appears to induce a dispersive phase transition process, as evidenced by the flattened and broadened dielectric platforms observed between T_s and T_m, accompanied by a significant reduction in dielectric loss (Fig. 2f, g). This phenomenon contributes to the attainment of narrower *P-E* loops with enhanced η[44,45]. In comparison to the BNSLT ceramics, the BNSLTMZ ceramics demonstrated a marked decrease in the T_s peak, which is crucial for promoting highly dynamic PNRs and modulating the relaxor response in BNT-based ceramics[46]. To further explore the domain dynamics, piezoresponse force microscopy (PFM) was utilized. In Fig. S8, the BNT ceramics exhibited long-range ordered ferroelectric domains with strong and distinct contrasts, which remained observable even after 20 min. In contrast, the polarization zones and piezoresponse in the BNSLT ceramics diminished within 4 min (Fig. 2h). Notably, the initial signal intensity of domains in the high S_{config} BNSLTMZ ceramics was significantly weaker, and these domains reverted to their original states within 2 min following the removal of the electric field (Fig. 2i). In summary, the proposed entropy-increase strategy effectively modulated the relaxor behavior in BNT-based ceramics. The high-entropy
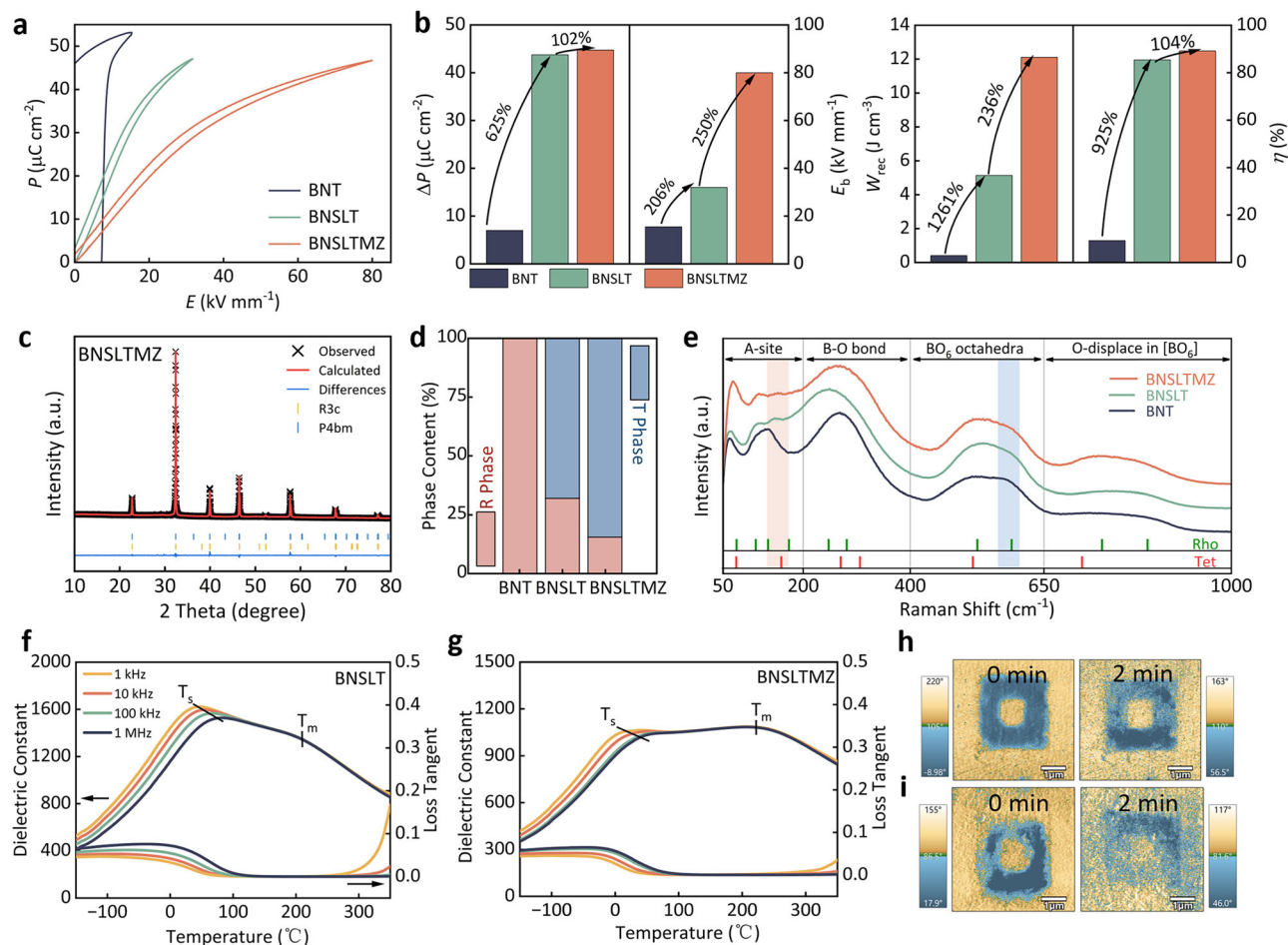
Fig. 2 | Effect of dual-step entropy-increasing design on dielectric properties, phase structure, and relaxor behavior of BNT-based bulk ceramics. a Unipolar *P-E* loops of the BNT, BNSLT, BNSLTMZ ceramics at their respective E_b. **b** Comparisons of ΔP and E_b, W_{rec} and η values among the BNT, BNSLT, and BNSLTMZ ceramics. **c** Rietveld refinement of XRD patterns of the BNSLTMZ ceramics. **d** Phase fractions of the BNT, BNSLT, and BNSLTMZ ceramics. **e** Normalized Raman spectra of the BNT, BNSLT, and BNSLTMZ ceramics under ambient temperature. Temperature-dependent dielectric constant and loss tangent of the as-sintered (**f**) BNSLT and (**g**) BNSLTMZ ceramics under various frequencies from 1 kHz to 1 MHz. Out-of-plane PFM phase pictures and domain evolution after different times for the (**h**) BNSLT and (**i**) BNSLTMZ ceramics under the field of 20 V.

BNSLTMZ component exhibited an increased proportion of relaxor phases, as well as an accelerated domain switching rate, resulting in reduced P_r, and more refined *P-E* loops. Such characteristics contributed to the exceptional energy storage efficiency in the fabricated MLCCs.

Structural origin of enhanced energy storage performance

To gain deeper insights into the relationship between local structure and enhanced ESP of the BNSLTMZ component, we conducted transmission electron microscopy (TEM) analysis of the BNSLTMZ ceramics, including bright-field imaging and selected area electron diffraction (SAED) along the $[001]_C$ and $[110]_C$ zone axes (Fig. 3a, b). The bright-field image displayed numerous fine bright and dark stripes, which are indicative of the presence of PNRs[47]. The formation of these PNRs is facilitated by compositional inhomogeneity resulting from increased S_{config}. Weak 1/2(*ooe*) superlattice diffraction spots were observed along the $[100]_C$ direction (Fig. 3a), corresponding to the *R3c* symmetry. Furthermore, distinct 1/2(*ooo*) superlattice diffraction spots were identified along the $[110]_C$ direction (Fig. 3b), which are associated with the *P4bm* symmetry[48]. These findings were consistent with the mixed-phase results obtained from XRD and Raman spectroscopic analyses.

The origin of relaxor behavior at the atomic scale was elucidated by acquiring atomic-resolution images of BNSLTMZ ceramics along

the $[100]_C$ zone axis using aberration-corrected high-angle annular dark-field scanning transmission electron microscopy (HAADF-STEM). The polarization displacement vectors of the A-site cations were calculated based on the centers of four adjacent B-site cations (arrows in Fig. 3c)[47]. Mapping of the cation displacement vectors revealed significant local fluctuations in both the orientation and magnitude of polarization (Fig. 3d). Notably, the variations in the direction and magnitude of these displacement vectors facilitated a clear differentiation among different nanodomains (selected regions in Fig. 3c), including T (orange regions), R (green regions), and C (blue regions) phases. These existing polymorphic domain regions exhibit inconsistent responses under electric fields, necessitating a higher electric field to drive all domains into a state of saturation polarization, thereby delaying polarization saturation. Furthermore, the diverse polarization configurations enhance both the directionality and intensity of polarization, resulting in a pronounced polarization response[49]. This enhancement contributes to the maintenance of a high P_m. Additionally, transition regions distinct from the R, T, and C phases were identified, as evidenced by the polarization vector distribution in Fig. 3g. These transition zones are believed to facilitate polarization rotation by bridging coexisting multiphase nanodomains, while simultaneously reducing both polarization anisotropy and domain-switching energy barriers[50]. From a quantitative perspective, the polarization vector distribution was analyzed by normalizing the
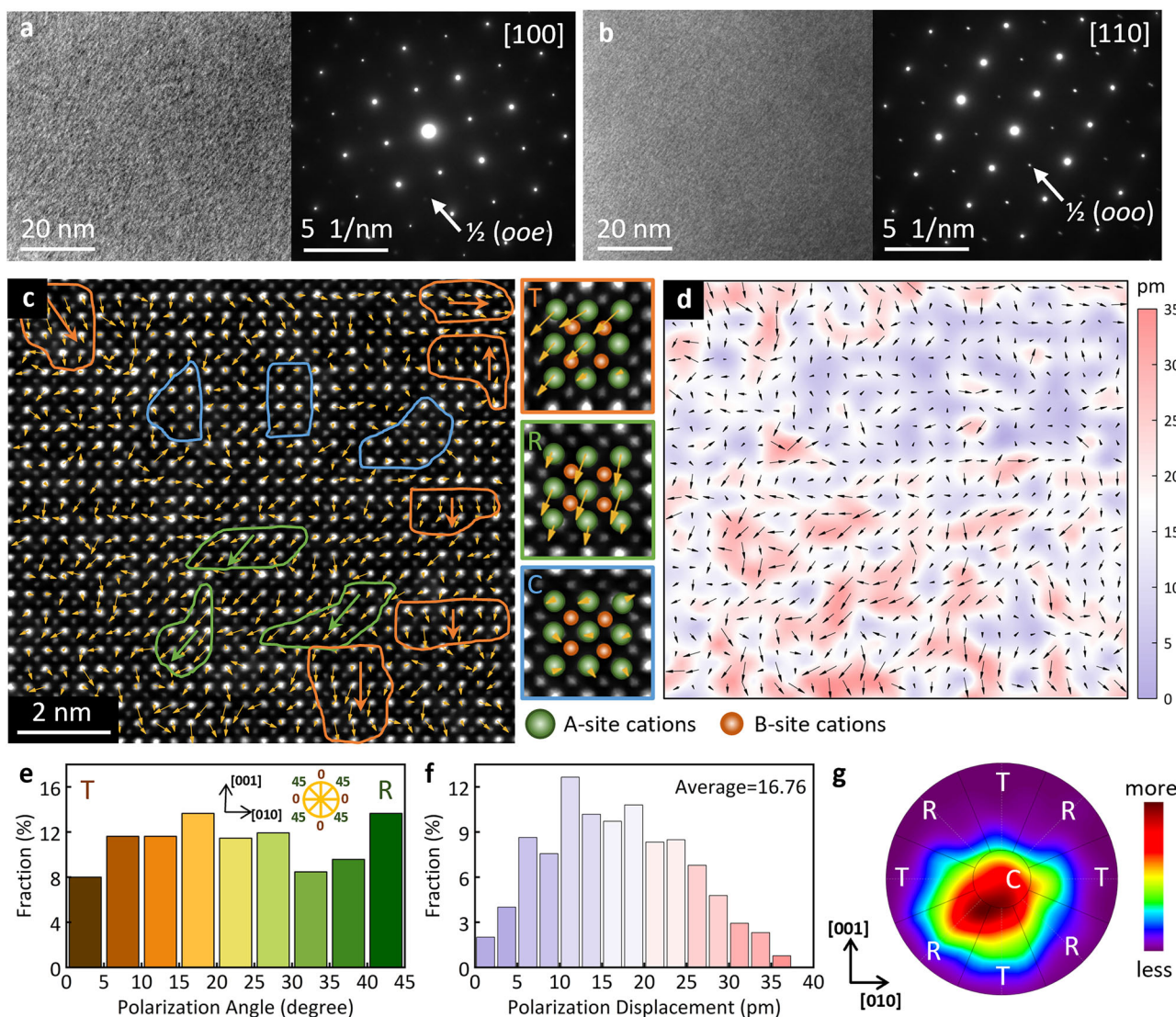
Fig. 3 | Structure analysis of the high-entropy sample. Bright-field TEM images and SAED patterns of the BNSLTMZ ceramics taken from (**a**) the $[001]_C$ zone axis and (**b**) the $[110]_C$ zone axis. HAADF-STEM images of (**c**) the BNSLTMZ ceramics, recorded along the $[100]_C$ zone axis, and magnified images of selected areas from (**c**) representing R, T, and C nanodomains respectively. The yellow arrows show the displacement of A-site cation in each unit cell, and the green and orange spheres representing A- and B-site cations, respectively. **d** The cation displacement vector mapping. Statistical distribution of (**e**) polarization angle and (**f**) polarization magnitude. **g** Statistical distribution of the amplitude and angle of the polarization vector.

angles to 0° for the T phase and 45° for the R phase (Fig. 3e). The nearly uniform angular distribution corroborates the presence of weak polarization anisotropy. Moreover, the average polarization displacement was measured and calculated to be 16.76 pm (Fig. 3f). Under an external electric field, these small-magnitude polarization responses not only effectively mitigate internal stress but also exhibit rapid recovery upon field removal. This behavior is consistent with the results obtained from PFM and is attributed to lower energy barriers for polarization reorientation[51]. In conclusion, in the high-S_{config} BNSLTMZ component, the coexistence of polymorphic domains significantly delays polarization saturation while preserving a high P_m. Simultaneously, the statistically anisotropic weak polarization vector and the transitional regions between polymorphic domains substantially reduce hysteresis loss.

We quantitatively evaluated the lattice distortion in the BNSLTMZ component by analyzing the c/a ratio derived from HAADF-STEM measurements (Fig. 4a)[13]. Compared to the BNT component, the mean c/a ratio for the BNSLTMZ component varied considerably, from 1.23 (Tab. S1) to 1.02, displaying random (Fig. 4a) and discrete distributions with a large standard deviation of 0.040 (Fig. S9). This pronounced lattice distortion originates from the high-S_{config}-induced atomic disorder, which simultaneously elevates the energy barrier for grain growth[52]. Consistent with this mechanism, SEM images and corresponding grain size (G) distributions (Fig. 4b) indicate a significant reduction in the average grain size from 2.01 μm to 0.67 μm with increasing S_{config}. The resultant fine-grained microstructure enhanced electrical resistance, increasing from 80 to 450 kΩ (Fig. 4c), while maintaining exceptionally low conductivity across a broad temperature range (Fig. S10a). Moreover, the appearance of the single Z″ and M″ Debye peaks at nearly the same frequency (Fig. S10b) illustrated the superior electrical homogeneity of BNSLTMZ ceramics. Consequently, the leakage current density reduced from 8.3×10^{-8} to 8.1×10^{-9} A cm^{-2} (Fig. S10c). The E_b is generally inversely proportional to the G ($E_b \propto (G)^{-\alpha}$)[53]. A statistical analysis of E_b for the BNT, BNSLT, and BNSLTMZ ceramics and the MLCCs was subsequently conducted using a two-parameter Weibull distribution fitting (Fig. 4d). The calculation can be expressed as follows: $p(E) = 1 - \exp(-(E/E_b)^\beta)$, where $p(E)$ presents the cumulative probability of electric breakdown at E and E_b is
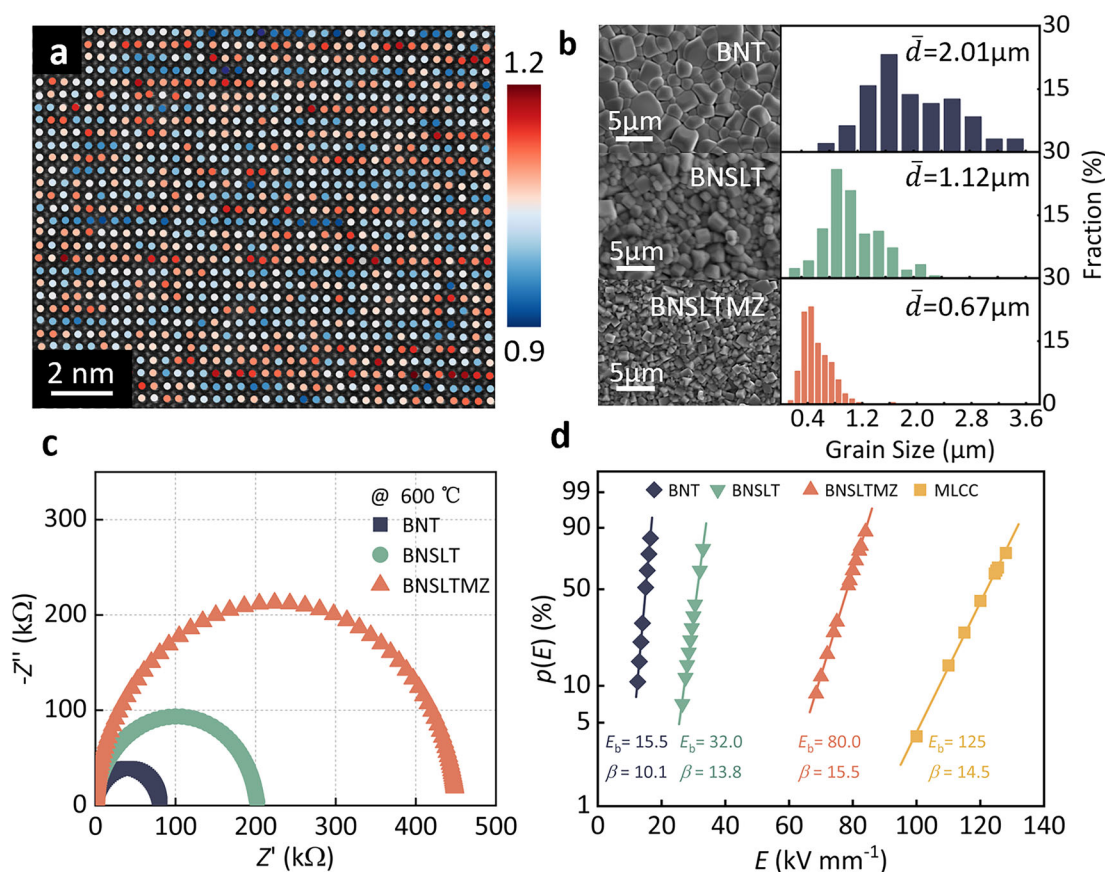
Fig. 4 | Lattice distortion, and electric resistance of entropy-assisted BNT-based ceramics and MLCCs. a The unit cell c/a ratios of the BNSLTMZ ceramics along the [100]$_c$ zone axis, the color of the circles indicates the c/a ratio for each unit cell. **b** SEM images and grain size distributions of the BNT, BNSLT, and BNSLTMZ ceramics, $\bar{d}$ represents the average grain size. **c** Impedance spectra of the BNT, BNSLT, and BNSLTMZ ceramics at 600 °C. **d** Weibull distribution analysis of the breakdown strength of the BNT, BNSLT, and BNSLTMZ ceramics and MLCCs.

the statistical breakdown strength corresponding to p(E) = 63.2%[19]. The Weibull modulus β for all samples exceeds 10, which indicates a high level of reliability. Concurrently, the E_b values of these BNT-based ceramics exhibited a significant increase with higher S_{config} values. Notably, the high-S_{config} MLCCs demonstrated an exceptionally high E_b value of 125 kV mm⁻¹. Collectively, our entropy-assisted strategy can effectively regulate the microstructure and synergistically improve the W_{rec} and η, ultimately achieving unprecedented ESP in MLCCs.

Stability and charge-discharge performance of entropy-assisted MLCCs

To further assess the potential applicability of the fabricated MLCCs, their ESP was evaluated under various conditions. In Fig. 5a and S12a, the MLCCs demonstrated excellent thermal stability across a broad temperature range of 0-100 °C, maintaining W_{rec} and η at 12.80 ± 0.15 J cm⁻³ and $95.49 \pm 1.11\%$, respectively. To investigate the structural origin of such thermal stability, temperature-dependent Raman spectroscopy and XRD measurements of BNSLTMZ ceramics were performed. In the temperature range from -180 °C to 180 °C, the number of Raman peaks remained almost unchanged, suggesting that the overall structural symmetry was stable over a wide temperature range[21] (Fig. 5b). As the temperature increased to around 0 °C, the Raman peak at approximately 585 cm⁻¹, associated with the E(LO8) mode of the $R3c$ phase, decreased in intensity, while the peak at around 520 cm⁻¹ redshifted slightly (Fig. S11a). This indicated the phase composition transition from an R-rich phase to a T-rich phase, which

was consistent with the results of the dielectric temperature spectrum (Fig. 2g), further validated the relaxor behavior observed in the dielectric measurements. Meanwhile, the absence of significant variations in XRD patterns across the temperature range from 0 °C to 180 °C (Fig. S11b, c) demonstrated the exceptional crystal structural stability of BNSLTMZ ceramics, which was likely responsible for their great thermal stability. Additionally, the MLCCs exhibited exceptional frequency stability across a frequency spectrum of 10-100 Hz, with W_{rec} and η exhibiting minimal variations of 12.84 ± 0.13 J cm⁻³ and $95.87 \pm 1.49\%$, respectively (Fig. 5c and S12b). Moreover, the MLCCs also demonstrated excellent fatigue resistance, maintaining stable ESP after 10⁶ cycles of measurement, as evidenced by W_{rec} and η variations of 12.85 ± 0.14 J cm⁻³ and $95.65 \pm 1.65\%$, respectively (Fig. 5d and S12c). Collectively, these results underscore the promising potential of MLCCs for practical energy storage applications in harsh external environments.

The practical charge-discharge performance of the MLCCs was evaluated under both overdamped (Fig. 5e, f) and undamped conditions (Fig. 5g). The time (t) - dependent discharge energy density (W_d) of the MLCCs can be determined as follows: $W_d = \frac{R \int I^2(t)dt}{V}$, where R represents the load resistance (100 Ω), I represents the overdamped discharging current, and V represents the effective volume of the tested samples[54]. The discharge speed $t_{0.9}$, defined as the time required for the discharged energy to reach 90% of its final value[20], was also extracted. The results indicated that the MLCCs exhibited a high W_d
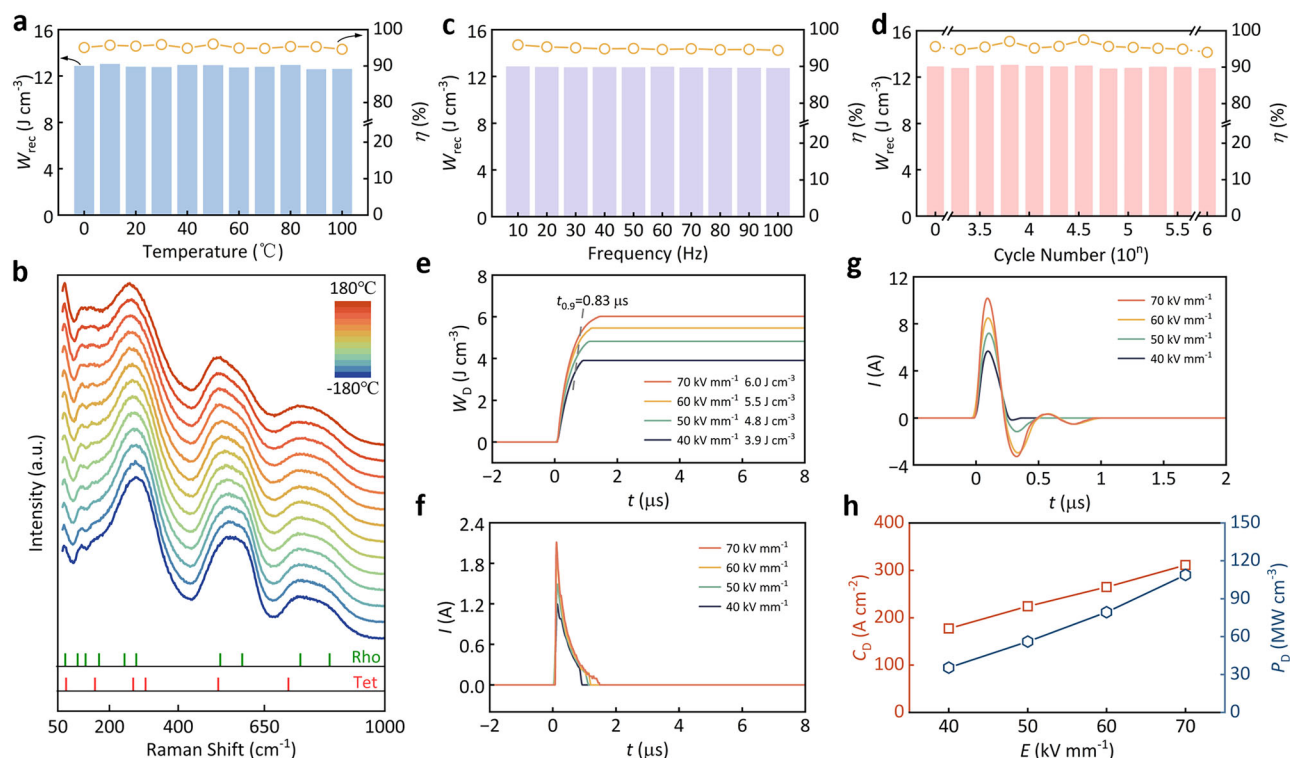
Fig. 5 | Evaluation of the stability and charge-discharge performance of the BNSLTMZ MLCCs. a Temperature-dependent evolution of W_{rec} and η of the MLCCs. **b** Raman spectra of the BNSLTMZ bulk ceramics under various temperature from -180 °C to 180 °C. **c** Frequency-, and (**d**) cycling-dependent evolution of W_{rec} and η of the MLCCs. Time-dependent (**e**) discharge energy density and (**f**) overdamped discharge current curves under various electric fields from 40 kV mm^{-1} to 70 kV mm^{-1}. **g** Undamped discharge curves under various electric fields from 40 kV mm^{-1} to 70 kV mm^{-1}. **h** Evolution of C_D and P_D values with respect to the electric field.

exceeding 5.6 J cm^{-3} under an electric field of 70 kV mm^{-1}, accompanied by a short $t_{0.9}$ of 0.83 μs. Furthermore, the current density (C_D) and power density (P_D) can be calculated using the formulas: $C_D = I_{max}/S$, $P_D = EI_{max}/2S$, where I_{max}, S, and E represent the positive current peak, the effective electrode area, and the applied electric field, respectively[23]. At 70 kV mm^{-1}, the MLCCs achieved a high C_D of 311 A cm^{-2} and an exceptional P_D of 108 MW cm^{-3} (Fig. 5h). In conclusion, the MLCCs demonstrated fast discharge speed, high discharge energy density, and high current and power densities. These advancements highlight the significant superiority of MLCCs for high-power energy storage applications.

In summary, a novel stepwise dual-site entropy-assisted engineering strategy was proposed to significantly enhance the energy storage performance of BNT-based lead-free MLCCs. This method effectively modulates both phase evolution and relaxor ferroelectric behavior, enabling the high S_{config} MLCCs to achieve an excellent W_{rec} of 17.8 J cm^{-3} and a high η of 97.6%. Atomic-scale analyses confirm that the coexistence of rhombohedral, tetragonal, and cubic polymorphic domains plays a crucial role in delaying polarization saturation while maintaining a high P_m. Additionally, the entropy-induced non-periodic lattice distortions contribute to grain refinement and improved electrical resistance, leading to a substantial increase in E_b. Beyond these core performance metrics, the MLCCs exhibited great operational stability across a wide range of temperatures, frequencies, and fatigue cycles, highlighting their robustness in demanding environments. Overall, the research presents a high-performance, environmentally sustainable material suitable for advanced pulsed power applications and establishes a versatile, practical design strategy for developing next-generation relaxor ferroelectric materials with enhanced energy storage characteristics.

Methods

Ceramic preparation

The BNT, BNSLT, and BNSLTMZ ceramics were synthesized through a conventional solid-state reaction method. The raw materials, including Bi_2O_3 (99.9%), Na_2CO_3 (99.8%), $SrCO_3$ (99.95%), La_2O_3 (99.99%), TiO_2 (99.5%), MgO (99.99%), ZrO_2 (99.99%), were first dried at 100 °C for 10 h. Subsequently, they were weighed precisely according to the stoichiometric composition and then planetary-ball-milled with ethanol for 24 h. The ball-to-powder ratio was set at 3:1, and the rotational speed was maintained at 400 r/min. After drying at 80 °C, the milled powders were calcined at 840-860 °C for 3 h, with the ramp rate of 2 °C/min. The calcined powders were then re-milled and dried under the same condition. Next, the 5 *wt*% polyvinyl alcohol (PVA) was added as a binder. The powders, with the aid of PVA, were pressed into pellets with a thickness of 1.5 mm and a diameter of 11.5 mm, which were achieved by cold isostatic pressing under a pressure range of 180-200 MPa. Subsequently, the pellets were heated to 500 °C for 3 h to remove the binder. To minimize the vaporization of Bi and Na elements, the pellets were buried in the powder of the same composition and then sintered at 1140-1160 °C for 2 h, with the ramp rate of 2 °C/min. For P-E loops and charge-discharge measurement, the pellets were polished to a thickness of 0.06 mm, and Au electrodes with an area of 0.785 mm^2 were sputtered. For dielectric measurement, the fabricated samples were polished to a thickness of 0.6 mm, coated with a silver electrode with a diameter of 8 mm on both surfaces, and sintered at 650 °C for 30 min.

MLCC fabrication

The same powder synthesized for ceramics preparation was mixed with solvents, dispersants, and plasticizers for 24 h to prepare the tape-casting slurry. The slurry was then defoamed under vacuum and cast

into a ~ 6 µm thick tape. After drying, the tape was cut and screen-printed with 70Ag/30 Pd electrodes. Blank tapes and electrode-printed tapes were stacked layer by layer according to the MLCC design specifications. The stacked layers were isostatically laminated at 70 °C and 64 MPa for 20 min and then cut into individual blocks. The blocks were heated to 270 °C following a 48 h warming period and held at that temperature for 2 h to remove the organic binder. They were then sintered at 1070 °C for 2 h, with a ramp rate of 25 °C/min to form the final MLCC structures.

Structural characterization

The crystal structure was analyzed using an X-ray diffractometer (XRD, D2 PHASER, Bruker, USA) with Cu K_a radiation (λ = 1.5406 Å). Raman spectroscopic analysis was carried out using a Raman spectrometer (inVia Reflex, Renishaw, UK) with an excitation wavelength of 532 nm. The domain structure and behavior were evaluated on the polished samples at ambient temperature through the use of a Piezoresponse Force Microscopy (PFM, Jupiter XR, Oxford Instruments, UK) under a voltage of 20 V. The microstructure was observed and recorded by tungsten filament scanning electron microscopy (SEM, SU3500, Hitachi, Japan) and transmission electron microscope (TEM, JEM-F200, JEOL, Japan). The average grain size and the grain distribution were analyzed by the software ImageJ. In addition, the atomic-scale structure was obtained using a Cs-corrected high-angle annular dark-field scanning transmission electron microscopy (HAADF-STEM, FEI spectra 300, Thermo Scientific, USA). The atomic positions were extracted after applying a Gaussian filter, with the assistance of the CalAtom software[55]. Subsequently, the centers of the A- and B-site cation columns were precisely located through two-dimensional Gaussian function fitting.

Property measurement

The temperature- and frequency-dependent dielectric properties, as well as the complex impedance, were evaluated by a precise LCR meter (E4980A, Agilent, USA). A ferroelectric measurement system (Premier II, Radiant, USA) was employed to record the *P-E* loops, with a test frequency of 10 Hz. The charge-discharge tests under both over-damped with a load resistance of 100 Ω and underdamped conditions were measured by a commercial charge-discharge platform (CFD-003, Gogo Instruments Technology, China).

Data availability

All data supporting this study and its findings are available within the article and its Supplementary Information. The data that support the findings of this study are available on request from the corresponding authors.

References

1. Luo, H. et al. Outstanding energy-storage density together with efficiency of above 90% via local structure design. *J. Am. Chem., Soc.* **146**, 460–467 (2024).
2. Long, C. et al. $Bi_{0.5}Na_{0.5}TiO_3$-based energy storage ceramics with excellent comprehensive performance by constructing dynamic nanoscale domains and high intrinsic breakdown strength. *Nano Energy* **124**, 109493 (2024).
3. Wang, X. et al. Machine learning assisted composition design of high-entropy Pb-free relaxors with giant energy storage. *Nat. Commun.* **16**, 1254 (2025).
4. Sun, Z. et al. Superior capacitive energy-storage performance in Pb-free relaxors with a simple chemical composition. *J. Am. Chem. Soc.* **145**, 6194–6202 (2023).
5. Liu, M. et al. Weakly coupled relaxor construction in lead-free ferroelectrics with simple composition for superior energy-storage performance. *Mater. Horiz.* **12**, 3939–3948 (2025).
6. Yang, B. et al. Engineering relaxors by entropy for high energy storage performance. *Nat. Energy* **8**, 956–964 (2023).
7. Pan, H. et al. Ultrahigh energy storage in superparaelectric relaxor ferroelectrics. *Science* **374**, 100–104 (2021).
8. Kim, J. et al. Ultrahigh capacitive energy density in ion-bombarded relaxor ferroelectric films. *Science* **369**, 81–84 (2020).
9. Shu, L. et al. Partitioning polar-slush strategy in relaxors leads to large energy-storage capability. *Science* **385**, 204–209 (2024).
10. Yang, K. et al. Excellent energy storage performance in $Bi_{0.5}Na_{0.5}TiO_3$-based lead-free high-entropy relaxor ferroelectrics via B-site modification. *J. Adv. Ceram.* **13**, 345–353 (2024).
11. Zhang, L. et al. Ultra-weak polarization-strain coupling effect boosts capacitive energy storage. *Adv. Mater.* **36**, 2406219 (2024).
12. Peng, H. et al. High-entropy relaxor ferroelectric ceramics for ultrahigh energy storage. *Nat. Commun.* **15**, 5232 (2024).
13. Zhang, M. et al. Ultrahigh energy storage in high-entropy ceramic capacitors with polymorphic relaxor phase. *Science* **384**, 185–189 (2024).
14. Chen, Y., Qi, J., Zhang, M., Luo, Z. & Lin, Y. H. Pyrochlore-based high-entropy ceramics for capacitive energy storage. *J. Adv. Ceram.* **11**, 1179–1185 (2022).
15. Sarkar, A. et al. High-entropy oxides: fundamental aspects and electrochemical properties. *Adv. Mater.* **31**, 1806236 (2019).
16. Kumar, A. et al. Atomic-resolution electron microscopy of nanoscale local structure in lead-based relaxor ferroelectrics. *Nat. Mater.* **20**, 62–67 (2021).
17. Li, D. et al. Atomic-scale high-entropy design for superior capacitive energy storage performance in lead-free ceramics. *Adv. Mater.* **37**, 2409639 (2025).
18. Zhou, S. et al. Microstructure and dielectric properties of high entropy $Ba(Zr_{0.2}Ti_{0.2}Sn_{0.2}Hf_{0.2}Me_{0.2})O_3$ perovskite oxides. *Ceram. Int.* **46**, 7430–7437 (2020).
19. Yang, B. et al. High-entropy enhanced capacitive energy storage. *Nat. Mater.* **21**, 1074–1080 (2022).
20. Lv, Z. et al. $NaNbO_3$-based multilayer ceramic capacitors with ultrahigh energy storage performance. *Adv. Energy Mater.* **14**, 2304291 (2024).
21. Wang, S. et al. Embedding plate-like pyrochlore in perovskite phase to enhance energy storage performance of BNT-based ceramic capacitors. *Adv. Energy Mater.* **15**, 2403926 (2025).
22. Zhao, P. et al. High-performance relaxor ferroelectric materials for energy storage applications. *Adv. Energy Mater.* **9**, 1803048 (2019).
23. Tang, T. et al. Self-generated glass-ceramics-like structure boosts energy storage performance of $AgNbO_3$-based MLCC. *Adv. Funct. Mater.* https://doi.org/10.1002/adfm.202425711 (2025).
24. Li, J., Li, F., Xu, Z. & Zhang, S. Multilayer lead-free ceramic capacitors with ultrahigh energy density and efficiency. *Adv. Mater.* **30**, 1802155 (2018).
25. Wang, G. et al. Ultrahigh energy storage density lead-free multilayers by controlled electrical homogeneity. *Energy Environ. Sci.* **12**, 582–588 (2019).
26. Cai, Z. et al. High-temperature lead-free multilayer ceramic capacitors with ultrahigh energy density and efficiency fabricated via two-step sintering. *J. Mater. Chem. A* **7**, 14575–14582 (2019).
27. Wang, G. et al. Fatigue resistant lead-free multilayer ceramic capacitors with ultrahigh energy density. *J. Mater. Chem. A* **8**, 11414–11423 (2020).
28. Bian, H. et al. Temperature-insensitive and high-energy storage performance in lead-based antiferroelectric multilayer ceramic capacitors. *Mater. Lett.* **382**, 137931 (2025).
29. Li, Y. et al. Enhanced energy storage performance in NBT-based MLCCs via cooperative optimization of polarization and grain alignment. *Nat. Commun.* **15**, 8958 (2024).
30. Wang, Z. et al. Ultra-high energy storage in lead-free $NaNbO_3$-based relaxor ceramics with directional slush-like polar structures design. *Nat. Commun.* **16**, 2892 (2025).

31. Yang, Y. et al. Giant energy storage density with ultrahigh efficiency in multilayer ceramic capacitors via interlaminar strain engineering. *Nat. Commun.* **16**, 1300 (2025).

32. Zhu, L. F. et al. Heterovalent-doping-enabled atom-displacement fluctuation leads to ultrahigh energy-storage DENSITY IN AgNbO₃-based multilayer capacitors. *Nat. Commun.* **14**, 1166 (2023).

33. Liu, J. et al. Near-zero energy dissipation multilayer ceramic capacitors via inhomogeneous polarization design. *Small* https://doi.org/10.1002/smll.202501062 (2025).

34. Liu, X., Li, Y., Sun, N. & Hao, X. High energy-storage performance of PLZS antiferroelectric multilayer ceramic capacitors. *Inorg. Chem. Front.* **7**, 756–764 (2020).

35. Li, J. et al. Grain-orientation-engineered multilayer ceramic capacitors for energy storage applications. *Nat. Mater.* **19**, 999–1005 (2020).

36. Malik, R. A. et al. Thermal-stability of electric field-induced strain and energy storage density in Nb-doped BNKT-ST piezoceramics. *J. Eur. Ceram. Soc.* **38**, 2511–2519 (2018).

37. Bin, C. et al. Improved energy storage performance in rare-earth modified lead-free bnt-based relaxor ferroelectric ceramics. *Appl. Phys. Lett.* **123**, 012901 (2023).

38. Zhu, L. F., Zhang, B. P., Li, S., Zhao, L., Wang, N. & Shi, X. C. Enhanced piezoelectric properties of Bi(Mg₁/₂Ti₁/₂)O₃ modified BiFeO₃–BaTiO₃ ceramics near the morphotropic phase boundary. *J. Alloy. Compd.* **664**, 602–608 (2016).

39. Jain, R. uth & Sundarakannan, D. E. B. Structural and Raman Spectroscopic Studies of Poled Lead-Free Piezoelectric Sodium Bismuth Titanate Ceramics. *Ceram. Int.* **42**, 4775–4778 (2016).

40. Tao, H. et al. Reversible evolution of ferroelectric-antiferroelectric phase transition in lanthanum-modified NaNbO₃-based ceramics. *J. Eur. Ceram. Soc.* **44**, 233–241 (2024).

41. Peña, M. A. & Fierro, J. L. G. Chemical structures and performance of perovskite oxides. *Chem. Rev.* **101**, 1981–2018 (2001).

42. Zhang, L., Pu, Y., Chen, M., Wei, T. & Peng, X. Novel Na₀.₅Bi₀.₅TiO₃ based, lead-free energy storage ceramics with high power and energy density and excellent high-temperature stability. *Chem. Eng. J.* **383**, 123154 (2020).

43. Yan, F. et al. Tape-casting lead-free dielectrics permit superior capacitive energy storage performance. *Adv. Energy Mater.* **15**, 2403535 (2025).

44. Luo, C. et al. Effect of Ca²⁺/Hf⁴⁺ modification at A/B sites on energy-storage density of Bi₀.₄₇Na₀.₄₇Ba₀.₀₆TiO₃ ceramics. *Chem. Eng. J.* **420**, 129861 (2021).

45. Wang, Z. et al. (Bi₀.₅Na₀.₅)TiO₃-based relaxor ferroelectrics with medium permittivity featuring enhanced energy-storage density and excellent thermal stability. *Chem. Eng. J.* **427**, 131989 (2022).

46. Yang, L. et al. Perovskite lead-free dielectrics for energy storage applications. *Prog. Mater. Sci.* **102**, 72–108 (2019).

47. Wang, S. et al. Temperature stability lock of high-performance lead-free relaxor ferroelectric ceramics. *Energy Storage Mater.* **66**, 103155 (2024).

48. Woodward, D. I & Reaney, I. M. Electron diffraction of tilted perovskites. *Acta Crystallogr. Sect. B* **61**, 387–399 (2005).

49. Duan, J. et al. High-entropy superparaelectrics with locally diverse ferroic distortion for high-capacitive energy storage. *Nat. Commun.* **15**, 6754 (2024).

50. Tao, H. et al. Ultrahigh performance in lead-free piezoceramics utilizing a relaxor slush polar state with multiphase coexistence. *J. Am. Chem. Soc.* **141**, 13987–13994 (2019).

51. Liu, H. et al. Chemical framework to design linear-like relaxors toward capacitive energy storage. *J. Am. Chem. Soc.* **146**, 3498–3507 (2024).

52. Huang, P. K. & Yeh, J. W. Inhibition of grain coarsening up to 1000 °C in (AlCrNbSiTiV)N superhard coatings. *Scr. Mater.* **62**, 105–108 (2010).

53. Peng, H. et al. Superior energy density achieved in unfilled tungsten bronze ferroelectrics via multiscale regulation strategy. *Adv. Sci.* **10**, 2300227 (2023).

54. Deng, T. et al. Ultrahigh energy storage performance in BNT-based binary ceramic via relaxor design and grain engineering. *Energy Storage Mater.* **71**, 103659 (2024).

55. Zhang, Q., Zhang, L. Y., Jin, C. H., Wang, Y. M. & Lin, F. CalAtom: a software for quantitatively analysing atomic columns in a transmission electron microscope image. *Ultramicroscopy* **202**, 114–120 (2019).

Acknowledgments

Author contributions

This work was conceived and designed by J.Q.L. and Z.L. J.Q.L. and Y.B.Z. Fabricated the ceramics, tested the energy storage, dielectric, structure, stability, and other properties, and processed related data, assisted by H.N.P. and L.L.W. J.Q.L., M.H.L., and S.G.Y. prepared the MLCC samples. Z.L., K.Y.Z. and H.R.Z. provided funds and laboratory equipment assistance. The manuscript was drafted by J.Q.L. and revised by Z.L., Z.P.Y., and G.S.W. All authors participated in the data analysis and discussions.

Competing interests

The authors declare no competing interests.

Additional information

Supplementary information The online version contains supplementary material available at https://doi.org/10.1038/s41467-025-63584-y.

Correspondence and requests for materials should be addressed to Zhen Liu, Huarong Zeng, Zupei Yang or Genshui Wang.

Peer review information *Nature Communications* thanks Rizwan Ahmed Malik, Mohan K. Bhattarai and the other, anonymous, reviewer(s) for their contribution to the peer review of this work. A peer review file is available.

Reprints and permissions information is available at http://www.nature.com/reprints

Publisher's note Springer Nature remains neutral with regard to jurisdictional claims in published maps and institutional affiliations.